How Fluid Pseudoplasticity and Elasticity Affect Propeller Flows in Biogas Fermenters

Markus Kolano*, Benjamin Ohnmacht, Andreas Lemmer and Matthias Kraume

DOI: 10.1002/cite.202400071

Dedicated to Prof. Dr.-Ing. Andreas Seidel-Morgenstern on the occasion of his retirement

Mixing in biogas fermenters is complex due to the non-Newtonian rheology of biogenic substrates, which exhibit both pseudoplasticity and elasticity. It is yet unclear how these non-Newtonian properties affect propeller flows and the mixing behavior in fermenters. Therefore, propeller flows in Newtonian as well as shear-thinning inelastic and elastic fluids are compared numerically and validated against particle image velocity (PIV) data. Elastic normal stresses lead to an increase of pumping rates in the laminar regime and a suppression of the formation of a propeller jet in the transitional regime. Thus, flow rates are severely overestimated by the inelastic, shear-thinning model in this regime. The results indicate that elasticity is critical for an accurate modeling of flows of biogenic substrates.

Keywords: Biogas fermenter, Computational fluid dynamics, Non-Newtonian rheology, Propeller flow, Viscoelasticity

Received: June 15, 2024; *revised:* August 05, 2024; *accepted:* August 08, 2024

1 Introduction

The most common mixing system in biogas fermenters consists of one or multiple propeller agitators. The mixing process is complex due to, e.g., the non-Newtonian rheology of biogenic substrates. Recent studies have shown that in addition to pseudoplasticity these substrates can also exhibit elastic properties. It is yet unclear how corresponding viscoelasticity influences propeller flows and as such the mixing behavior in biogas fermenters. This work, therefore, aims to analyze the effects of both pseudoplasticity and elasticity by comparing numerically obtained propeller flows of a Newtonian as well as shear-thinning fluids, for which both inelastic and elastic properties are considered. These fluids are examined in a single-propeller configuration, in which numerical results are also validated against experimental particle image velocimetry (PIV) data, as well as a stirred tank with multiple impellers.

1.1 Rheology of Biogenic Substrates

It has been demonstrated in several studies that the majority of biogenic substrates used in anaerobic digestion exhibit pseudoplasticity, i.e., the dynamic viscosity η of these substrates decreases with increasing shear rate $\dot{\gamma}$. A review of common measurement techniques and results is given in [1].

The elasticity of biogenic substrates, on the other hand, has been subject to a comparably few recent studies. Baudez et al. [2] applied oscillatory measurements in a rotational rheometer with a cylindrical Couette geometry to quantify the viscoelasticity of waste water treatment sludges before and after anaerobic digestion. For the digested sludge, e.g., frequency sweeps showed a characteristic relaxation time:

$$\lambda_\omega = \omega^{-1}_{|_{G'=G''}} \tag{1}$$

where G' is the storage, G'' is the loss modulus, and ω denotes the rotational frequency of about 2 s. Farno et al. [3] applied an analogous measurement technique to show the viscoelasticity of waste activated sludge. A plate-plate measurement system was used by Jiang et al. [4] in a rotational rheometer to analyze the viscoelasticity of digested sludges. Brehmer and Kraume [5, 6] applied the vane method [7] and relaxation tests to investigate the viscoelasticity of several biogenic substrates from industrial biogas plants. All analyzed substrates exhibit significant elasticity, as quantified by the ratio of loss to storage modulus G''/G' in the linear viscoelastic regime. Oscillatory measurements were also performed by [8] to highlight the viscoelastic characteristics of silage digestate.

[1]Markus Kolano (markuskolano@gmail.com),
[2]Benjamin Ohnmacht, [2]Dr. Andreas Lemmer,
[1]Prof. Dr.-Ing. Matthias Kraume
[1]Technische Universität Berlin, Fachgebiet Verfahrenstechnik, Ackerstr. 76, 13355 Berlin, Germany.
[2]Universität Hohenheim, Landesanstalt für Agrartechnik und Bioenergie, Garbenstr. 9, 70599 Stuttgart, Germany.

1.2 Propeller Flows in Non-Newtonian Fluids

Works dealing with propeller flows in non-Newtonian media are relatively sparse. Some research has been published in the context of pulp and paper industry, in which mainly the effects of yield stresses on side-entering propeller flows and the corresponding formation of caverns have been investigated [9–14]. In addition, there are several works analyzing axial impeller flows in shear-thinning, yield stress fluids in centrally stirred vessels, examples of which are in [15–20]. For the here presented work most relevant results are described in [21]. In this work, flow fields induced by a side-entering impeller were measured via PIV in shear-thinning Carbopol solutions exhibiting a yield-stress as well as a Newtonian glycerol solution. In the Newtonian fluid, high viscosities close to the impeller prevent a formation of an axial jet, so that a radial pumping effect is induced by the propeller for the analyzed stirring rates. In the pseudoplastic solutions, viscosities in the vicinity of the propeller can be low enough for inertial forces inducing axial flow components, leading to semi-radial discharge behavior and a recirculation zone in front of the impeller.

Works dealing with inelastic, shear-thinning fluids not exhibiting a yield stress have also been published. Brehmer et al. [22] described, i.a., the distinct influence of pseudoplasticity on propeller jet length via computational fluid dynamics (CFD) simulations. Reviol et al. [23] developed a design method for the geometrical optimization of propeller agitators under consideration of pseudoplasticity. Wang et al. [24] analyzed side-entry propeller flows of a shear-thinning carboxymethyl cellulose fluids via ultrasonic Doppler velocimetry. They found, i.a., a clear limitation of the propeller jet length for low stirring rates, which they accounted to the development of caverns. In addition, they also analyzed the effects of different turbulence models on propeller flows in shear-thinning fluids [25].

The influence of elasticity on side-entry propeller flows has also been investigated in recent studies. Brehmer was the first to find the changes of propeller flow behavior in shear-thinning, viscoelastic fluids [6]: For low stirring rates, an axial discharge behavior without the development of a jet is generated by propeller agitators. Increasing the stirring rate leads to a radial discharge behavior first, followed by successively more dominant axial flow components in combination with a recirculation zone until a fully developed axial jet is formed for high stirring rates. Kolano et al. [26] validated these results in a pilot-scale fermenter and additionally explained the changes in flow patterns by the ratio of elastic forces, induced by elastic normal stresses, to inertial forces. Additionally, Can and Kraume [27, 28] conducted similar research and found that the propeller discharge angle was dependent on whether a speed-up or -down operation mode was conducted. Hence, propeller flows in viscoelastic fluids can be affected by hysteresis. Further works on propeller flows in centrally stirred vessels showed, i.a., the distinct influence of viscoelasticity on the discharge angle [29, 30].

1.3 Simulating Flows in Biogas Fermenters

Numerous approaches have been applied to simulate the flow in biogas fermenters. As described in [31–36], the most common method is the consideration of pseudoplasticity as a generalized Newtonian fluid with varying viscosity functions such as power-law approaches and different turbulence models. Viscoelasticity has not been considered in any of these studies. Mixed results have been reported concerning quantitative agreement between model and experimental flow data [31–36].

Our own experiences with inelastic modeling approaches are depicted in Fig. 1. Here, three operation modes, i.e., agitation with just agitator 1, agitator 2, and both, in an industrial-scale biogas fermenter (see Fig. 1a) [37, 38] are simulated with different inelastic rheological models which are fitted to the kinematic viscosity ν of a biogenic substrate obtained in a tube viscosimeter (see Fig. 1b). Experimental data on flow velocities at two different measurement points, obtained via magnetic-inductive velocimetry [39], are then compared to the numerical data (see Fig. 1c). While all of the models are capable to qualitatively reproduce the flow features generated for the different operational modes, astonishingly high quantitative deviations are found; fluid velocities are overestimated by more than a factor of 10 in the simulations. Note that since these results are just given here as an example, further details on this study are not part of this paper, but can be found in the final report of the FNR project “Sens-O-Mix” [40].

1.4 Aim of this Work

It has been demonstrated that biogenic substrates exhibit both pseudoplastic and elastic flow properties. While some advances have been achieved concerning the experimental quantification of the effects these rheological properties have on propeller induced flows, the mechanisms are still not fully understood. Further, it has been found that inelastic, non-Newtonian modeling approaches can deviate substantially from experimental flow data in biogas fermenters. In this context, the influence of elasticity has not been tested at all. In the following, therefore, both inelastic and elastic modeling approaches are applied to simulate the flow induced by propellers. The aim is to achieve a better understanding of how these different rheological behaviors influence propeller flows and also to test if viscoelastic models are better suited to reproduce propeller flows in fluids exhibiting viscoelasticity than inelastic approaches.

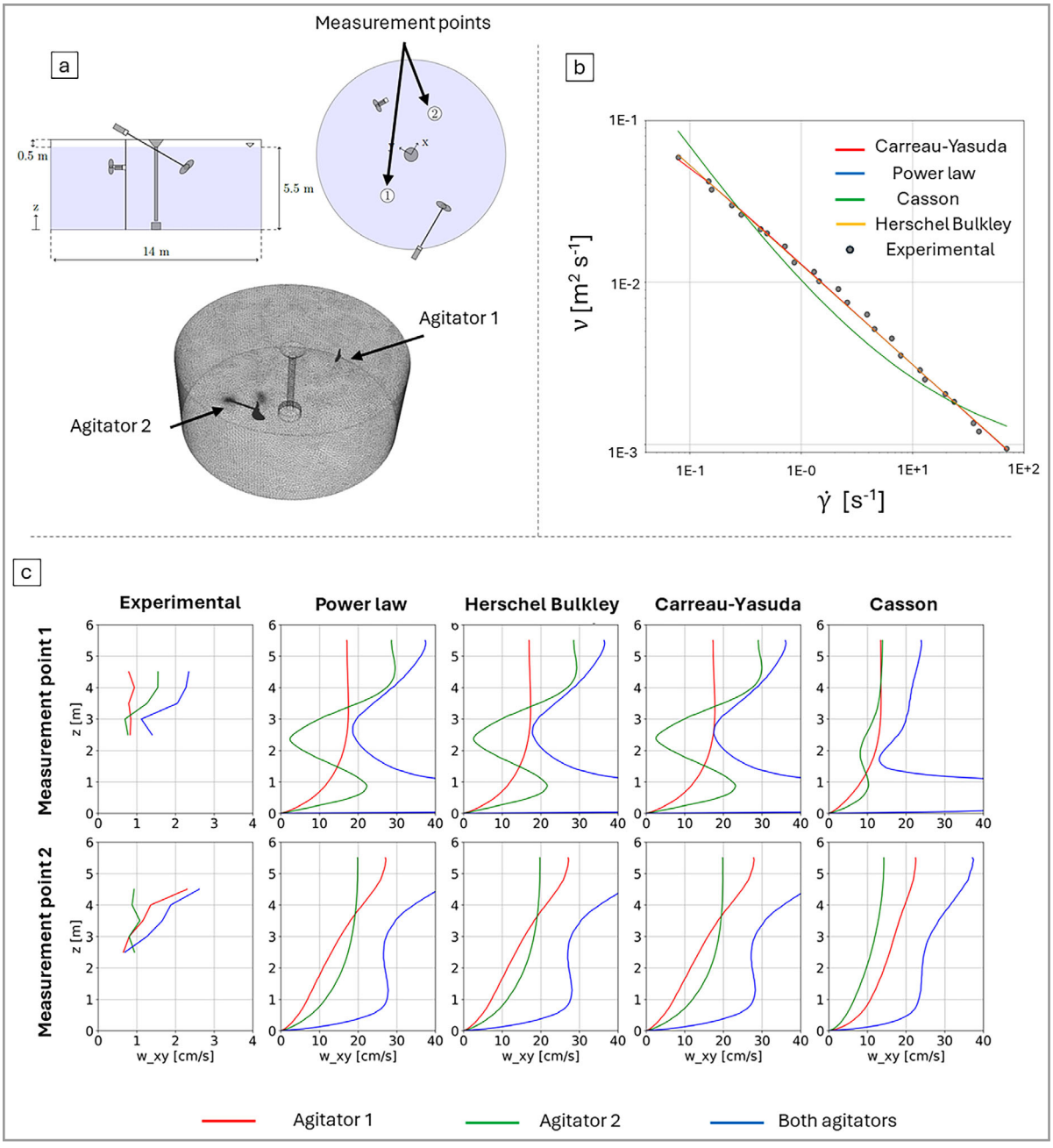

Figure 1. Schematic of an industrial-scale fermenter and corresponding CFD mesh (a); viscosity of a biogenic substrate and corresponding model fits (b); comparison of numerically and experimentally obtained velocity profiles. Note that the abscissa scale differs between experiments and simulations.

2 Theoretical Background

2.1 Modeling the Flow of (Non-)Newtonian Fluids

The modeling basis of all here analyzed fluids is a momentum conservation equation:

$$\rho\left(\frac{\partial \boldsymbol{w}}{\partial t} + \nabla \cdot \left(\boldsymbol{w}\boldsymbol{w}^{\mathrm{T}}\right)\right) = -\nabla p + \nabla \cdot \boldsymbol{\tau} \tag{2}$$

with density ρ, velocity vector $\boldsymbol{w}$, time t, pressure p, and stress tensor $\boldsymbol{\tau}$. This equation is coupled with the conservation of mass of an incompressible fluid:

$$\nabla \cdot \boldsymbol{w} = 0 \tag{3}$$

Different rheological behaviors are then considered in the determination of the stress tensor $\boldsymbol{\tau}$. For Newtonian fluids, $\boldsymbol{\tau}$ is derived from a constant dynamic viscosity (in this work

at zero shear rate) η_0 and the deformation rate tensor $\boldsymbol{D}$:

$$\boldsymbol{\tau} = 2\eta_0 \boldsymbol{D} = \eta_0 \left[\nabla \boldsymbol{w} + (\nabla \boldsymbol{w})^{\mathrm{T}}\right] \tag{4}$$

For the inelastic, shear-thinning fluid, a shear rate-dependent dynamic viscosity is considered in form of a generalized Newtonian fluid. Here, the three-dimensional deformation rate field is reduced to a scalar representative shear rate value by determining the second invariant of the rate of deformation tensor [41]:

$$\dot{\gamma} \equiv |\dot{\boldsymbol{\gamma}}| = \sqrt{2tr\,(\boldsymbol{D}\cdot\boldsymbol{D})} \tag{5}$$

This way, viscosity models like the Carreau-Yasuda model used in this work [42]

$$\eta = \eta_\infty + (\eta_0 - \eta_\infty)\left[1 + (\lambda_{\mathrm{CY}}\,\dot{\gamma})^a\right]^{\frac{n-1}{a}} \tag{6}$$

where η_∞ is the viscosity at infinity shear rate, λ_{CY} is the Carreau-Yasuda relaxation time, a and n are additional parameters, can be integrated in the determination of the stress tensor:

$$\boldsymbol{\tau} = 2\eta\,(\dot{\gamma})\,\boldsymbol{D} \tag{7}$$

For the viscoelastic fluid, the stress tensor is determined according to the extra-stress tensor approach [43]:

$$\boldsymbol{\tau} = \sum_{\mathrm{i}=1}^{\mathrm{N}} \boldsymbol{\tau}_{\mathrm{P,i}} + \boldsymbol{\tau}_{\mathrm{S}} \tag{8}$$

where $\boldsymbol{\tau}_{\mathrm{P;\,i}}$ represent N elastic modes and $\boldsymbol{\tau}_{\mathrm{s}}$ is an inelastic contribution. $\boldsymbol{\tau}_{\mathrm{s}}$ is modeled by Eq. (4); the elastic modes are represented in this work by the Giesekus model [44, 45]:

$$\boldsymbol{\tau}_{\mathrm{P,i}} = 2\eta_{\mathrm{P;i}}\boldsymbol{D} - \lambda_{\mathrm{i}}\check{\boldsymbol{\tau}}_{P,i} - \lambda_{\mathrm{i}}\frac{\alpha_{\mathrm{i}}}{\eta_{\mathrm{P,i}}}\left(\boldsymbol{\tau}_{\mathrm{P,i}}\cdot\boldsymbol{\tau}_{\mathrm{P,i}}\right) \tag{9}$$

with the relaxation time λ_{i} and the mobility factor α_{i}. $\check{\boldsymbol{\tau}}$ is the upper-convected derivate

$$\check{\boldsymbol{\tau}} = \frac{\partial}{\partial t}\boldsymbol{\tau} + \boldsymbol{w}\cdot\nabla\boldsymbol{\tau} - (\nabla\boldsymbol{w})^{\mathrm{T}}\cdot\boldsymbol{\tau} - \boldsymbol{\tau}\cdot(\nabla\boldsymbol{w}) \tag{10}$$

which is the time derivative of $\boldsymbol{\tau}$ in a reference frame rotating and stretching with the fluid.

2.2 Characteristics of a Stirred Tank

A common dimensionless number to evaluate whether flow is laminar or turbulent in a stirred vessel with inelastic fluids is the Reynolds number:

$$Re = \frac{\rho n d^2}{\eta} \tag{11}$$

with density ρ and agitator diameter d. Generally, laminar flows are obtained for $Re < 10$ and, depending on the mixing system, fully turbulent flows for $Re \gtrsim 10^4$ [46]. While the calculation of this number is simple for Newtonian fluids, fluids with a shear rate-dependent viscosity necessitate the coupling of stirring parameters and deformation rates. The most common approach to this, which is also applied in this study, is the Metzner-Otto concept:

$$\dot{\gamma} = k_{\mathrm{MO}}\,n \tag{12}$$

with the Metzner-Otto constant k_{MO} [47, 48]. This concept, therefore, assumes a linear relationship between stirring rate n and a representative shear rate with a proportionality constant which is dependent on the geometry of the agitation system. This relationship was also validated for a biogas geometry in the laminar regime [49]. As in other works [26], a $k_{\mathrm{MO}} = 10$ is assumed for the propellers used in this study.

A similar number to Re is the elasticity number [30, 50, 51]:

$$El = \frac{N_1}{\rho n^2 d^2} \tag{13}$$

While Re determines the ratio of inertial to viscous forces, El compares elastic to inertial forces. The elastic forces are here represented by the primary normal stress difference N_1, which is a characteristic property of an elastic fluid and the cause of phenomena like the Weissenberg effect or elastic flow compartmentalization [30, 52]. Since N_1 is also shear rate-dependent, the Metzner-Otto concept is applied for the calculation of El in this work as well. Another useful number to evaluate whether flows are more strongly influenced by elastic or viscous effects is the Weissenberg number [30, 50, 51]:

$$Wi = \frac{N_1}{\tau_{\mathrm{s}}} \tag{14}$$

with the shear stress $\tau_{\mathrm{S}} = \eta\,\dot{\gamma}$.

There are several dimensionless numbers describing the effectiveness of a stirred vessel [53]. One of the numbers used in this work is the pumping number:

$$Fl_{\mathrm{P}} = \frac{\dot{V}_{\mathrm{P}}}{n\,d^3} \tag{15}$$

which is the dimensionless form of the pumping rate $\dot{V}_{\mathrm{P}}$ of an agitator. The pumping rate is generally determined by integrating velocities $\boldsymbol{w}$ over characteristic surfaces A. To determine this rate for the propeller agitators used in this work, the axial velocity component w_z is integrated over a disk A_{D} with the same diameter as the propeller placed at the tip of the propeller hub.

$$\dot{V}_{\mathrm{P}} = \int_0^{A_{\mathrm{D}}} w_z\,(A)\;dA \approx \sum_{\mathrm{i}\,=\,1}^{\mathrm{N}} w_z\,(A)\,A_i \approx 2\pi \int_0^{d/2} w_z\,(r)\;r\,dr \tag{16}$$

Since data for the whole vessel volume are available in the CFD data, this is simply achieved by interpolating velocity cell values on a disk discretized by about $N = 1000$ elements and applying the sum given in Eq. (16). For the PIV method applied in this work, data is only determined in the radial-axial measurement plane (see Sect. 3.2). Hence,

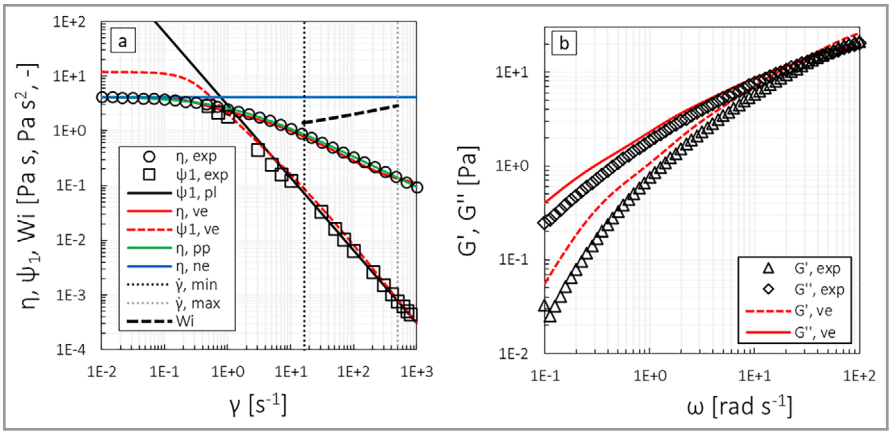

Figure 2. Rheology of the fluids in (a) steady shear and (b) oscillatory shear. Lines represent model functions.

the integral of the radial velocity profile $w_z(r)$ at the propeller hub, for which a continuous function is determined by fitting a polynomial of high order to the discrete velocity values, is calculated (cf. Eq. (16)). This is possible since phase-averaged flow fields are determined via PIV in this work (cf. Sect. 3.2).

The pumping rate does not include the fluid flow which is entrained by the propeller jet. The total rate of fluid flow in a vessel will, therefore, be higher in almost all cases. To determine the total (primary) circulation flow number

$$Fl_C = \frac{\dot{V}_C}{n\, d^3} \tag{17}$$

an area covering the whole (primary) circulating flow $\dot{V}_C$ needs to balanced. In this work, $\dot{V}_C$ is determined by summing up all products of the area elements with their normal velocity components on the cyclic boundary as explained in Sect. 3.3. This is valid since the center of the primary circulation vortex is located at the center of the vessel.

3 Materials and Methods

3.1 Fluids and Rheology

As in comparable works [22, 27, 28, 30, 52], the experiments on rheology and fluid dynamics in this work were all determined for an aqueous solution of carboxymethyl cellulose (CMC, 10 g kg^{-1}) in ultrapure water. A rotational rheometer (MCR 302, Anton Paar) with a cone-plate system (CP60) at a temperature of 20 °C was used for the measurements of rheological properties. Thereby obtained data are given for a shear rate sweep in Fig. 2a and for a frequency sweep in Fig. 2b. More details on the experimental procedure and additional rheological data can be found in [30].

The CMC solution is pseudoplastic, i.e., η decreases above a critical shear rate (cf. Fig. 2a). It also does not exhibit a yield stress; a Newtonian plateau is reached for small shear rates. Further, the solution is elastic, since it develops primary normal stress differences N_1 in simple shear flows as given by the primary normal stress coefficient $\psi_1 = N_1\dot{\gamma}^{-2}$ in Fig. 2a. In the shear rate range covered in the stirring experiments according to Metzner-Otto ($\dot{\gamma}_{min} \le n\ k_{MO} \le \dot{\gamma}_{max}$), $1.4 \le Wi \le 2.9$. Hence, N_1 are generally higher than shear stresses in the analyzed stirring rate range. In that range, a power-law (pl) approach $\psi_1 = a\dot{\gamma}^b$ with $a = 2.98\ Pa\ s^{3+b}$ and $b = -1.32$ is sufficiently accurate to correlate the normal stresses.

The elasticity of the fluid also leads to the development of storage moduli G' in the small amplitude oscillatory data in Fig. 2b. From these data, a characteristic relaxation time according to Eq. (1) of $\lambda_\omega = 0.025$ s can be derived. The fluid is, thus, only weakly elastic compared to the organic substrates which have been analyzed in literature (cf. Sect. 1.1). The effects of elasticity on propeller flows resulting from the CMC solution should, therefore, at least be relevant or even more pronounced for organic substrates.

In Fig. 2, model data are also given as lines. For the Newtonian fluid (ne), the viscosity of the Newtonian plateau is taken ($\eta_0 = 4.2$ Pa s). The inelastic, shear-thinning fluid (pp) is modeled by the Carreau-Yasuda equation (cf. Eq. (6)). Parameters for this model were obtained by least-squares regression and are $\eta_0 = 4.2$ Pa s, $\eta_\infty = 0$ Pa s, $\lambda = 0.88$ s, $a = 0.754$, and $n = 0.44$. For the elastic fluid (ve), parameters for the Giesekus model were generally derived by the method as described in [54] and are given in Tab. 1.

To obtain comparable viscosity curves between the pp and ve models, this method was adjusted by a last fitting step, in which all of the parameters of the Giesekus model are simultaneously fitted to an error function in which the viscosity error is weighted. Thus, comparable viscosity functions with an average, relative deviation of the ve to the pp model of 8 % are obtained. Analogous relative

Table 1. Parameters of the extra-stress tensor model. The last mode represents the inelastic contribution.

Mode i	Model	λ_i [s]	$\eta_{p,i}$; η_s [Pa s]	α_i
1	Eq. (9)	2.875	1.894	0.999
2	Eq. (9)	0.418	1.182	0.786
3	Eq. (9)	0.086	0.673	0.864
4	Eq. (9)	0.017	0.327	0.627
5	Eq. (9)	$2.9 \cdot 10^{-4}$	0.075	$2.85 \cdot 10^{-4}$
–	Eq. (4)	–	0.0154	–

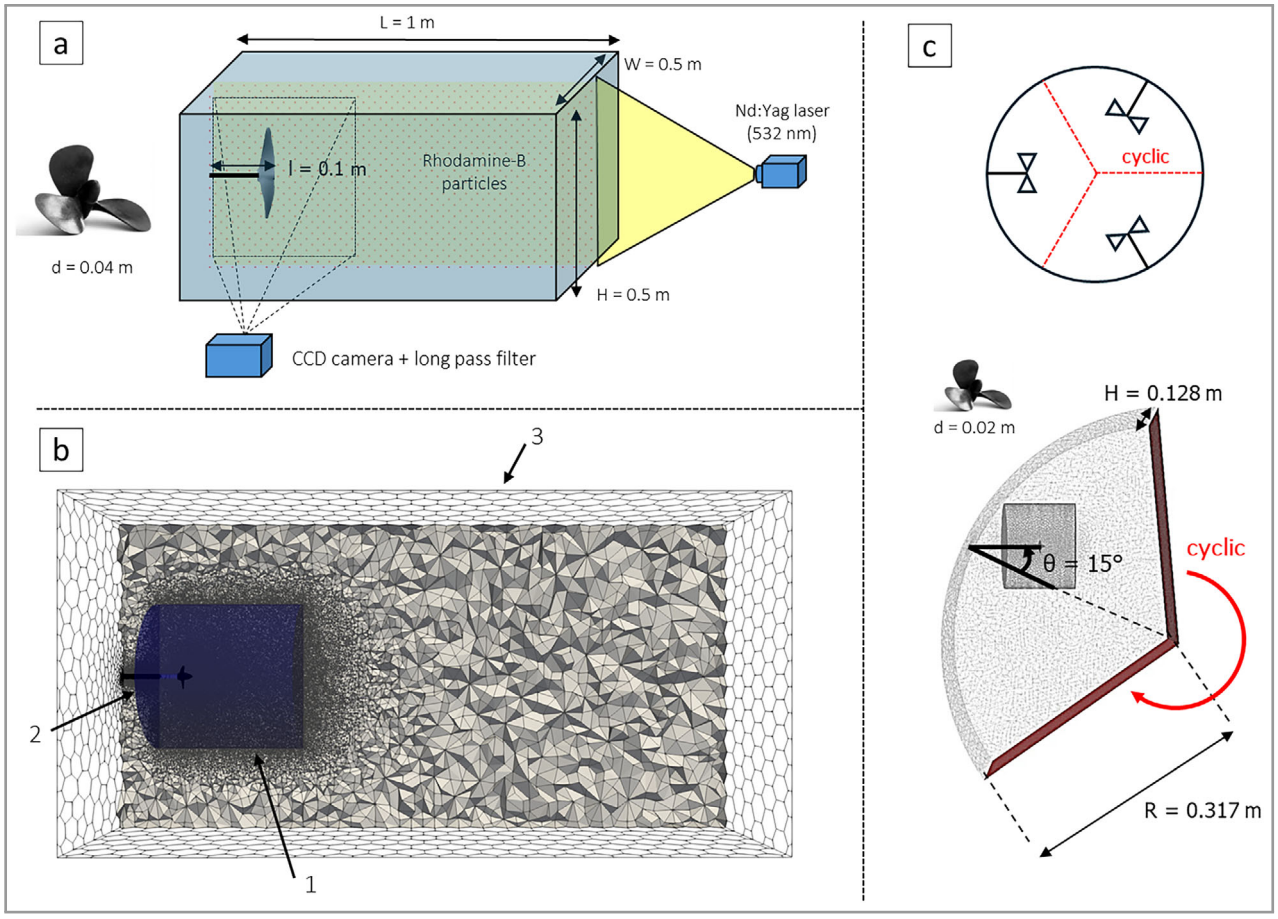

Figure 3. Experimental setup and propeller (a); mesh for single propeller configuration (b); congruent parts and mesh for the multipropeller configuration (c).

deviations to the experimental data are 8 % for ve and 1% for pp.

The ve model is also capable of reproducing the elastic properties of the fluid, albeit less quantitatively accurate (see Fig. 2). Mainly caused by data for $\dot{\gamma} < 10\ s^{-1}$, ψ_1 are generally overestimated with an average, relative deviation of 24 % to the measured normal stresses. Similarly, G' with 49 % and G'' with 21 % are both significantly overestimated, mostly for $\omega < 1\ rad\ s^{-1}$. These deviations are a consequence of the weighting of the viscosity error explained above and were accepted in order to achieve comparable viscosity functions between the models.

3.2 Experimental Setup

The stirring experiments were part of a published PhD thesis [6] and are, thus, just shortly summarized here. A cuboid glass tank with the dimensions 0.5 $L = W = H = 0.5$ m was used as stirred vessel (see Fig. 3a). This shape was chosen to minimize wall effects on the propeller jet flows. As agitator, a 3-bladed ship propeller (Graupner Modellbau) with a diameter $d = 0.04$ m was used. It was placed centrally regarding one short side of the vessel and leaped 0.1 m into the tank (see Fig. 3a).

For the PIV measurements, a double-pulsed ND:YAG laser (Litron Lasers, 532 nm) with a sheet optic was employed. The resulting light sheet was placed to illuminate the axial-radial plane as illustrated in Fig. 3a. Thus, the fluorescent light emitted by PIV tracer particles (PMMA containing rhodamine B, 50 µm) could be selectively recorded by a CCD camera with a long pass filter (> 540 nm). To obtain phase-averaged flow fields, 30 double-images were recorded for each stirring rate at varying impeller angles, correlated by a multipass PIV algorithm (DaVis 8.4), and finally arithmetically averaged. These 30 flow fields are sufficient to determine phase-averaged pumping rates, as discussed in Appendix A. The resolution of the flow field is 2.4 mm to 2.4 mm.

The stirring rate range of the PIV measurements is 100 rpm $\leq n \leq$ 3000 rpm. Hence, all stirring experiments were conducted in the shear-thinning range according to Metzner-Otto ($\dot{\gamma}_{min} \leq n\, k_{MO} \leq \dot{\gamma}_{max}$, see Fig. 2).

3.3 Numerical Setup

The CFD simulations were conducted in two geometries. For the single propeller case, a geometry equivalent to the experimental setup was used (see Fig. 3b). The second geometry represents a more realistic, i.e., industrially relevant scenario as it includes three agitators and a cylindrical vessel with a ratio of $H/D = 0.2$, which is common for industrial biogas fermenters (see Fig. 3c) [55–57]. Since the propellers were positioned at an azimuthal rotation of exactly 120° from another, the vessel could be split into three congruent parts. Using cyclic boundaries, it is, therefore, sufficient to simulate only one of those parts, thereby reducing numerical effort. The propellers ($d = 0.02$ m) were rotated with an azimuthal angle of $\theta = 15°$ compared to the radius axis intersecting the point of the propeller shaft entry and placed at $H/2$ with an insertion depth of 0.1 m. A 3D scan of the propeller used in the experiments allowed to accurately represent the agitator in both cases.

The meshes for both geometries were created using the commercial Software StarCCM+ (Version 14.04). The meshes were split into a rotating cylinder and a stationary part (cf. boundary 1 in Fig. 3b). A mesh independence study was not conducted; instead, mesh refinement parameters as well as the cell base size were equal to the mesh for which mesh independence in a similar numerical study was found [54]. With these parameters, a much finer resolution of the flow in the vicinity of the propeller is generated (cf. Fig. 3b). The resulting number of polyhedral cells is $432 \cdot 10^3$ for the single propeller and $76 \cdot 10^3$ for the multipropeller case.

To discretize and solve the equations systems described in Sect. 2.1, OpenFOAM (Version 2.3.1) was applied. For the inelastic models, the pimpleDyMFoam solver was utilized, which is a transient solver capable of handling dynamic meshes and generalized Newtonian fluids. For the viscoelastic fluid, a modified version of this solver including viscoelastic models [58] as described in [54] was taken. A sliding mesh approach was applied for all simulations.

As boundary conditions, spatial gradients of $\boldsymbol{\tau}$ and p were set to zero except for the interface between stationary and dynamic mesh parts (see boundary 1 in Fig. 3b), which was handled by the cyclicAMI boundary condition. For velocity $\boldsymbol{w}$, no-slip at stationary walls and a slip condition on the vessel surface (cf. boundary 3 in Fig. 3b) was applied. On rotating walls, fixed velocity values were set corresponding to the rotational frequency of the agitator and the radial distance to the axis of rotation (cf. boundary 2 in Fig. 3b).

The time step size was controlled by a maximum Courant number of $Co \leq 2$. Convergence within one time step was defined to be achieved if residua smaller than 10^{-4} for p and $\boldsymbol{\tau}$ and 10^{-5} for $\boldsymbol{w}$ were reached. All simulations were run until stationary pump and circulation rates were obtained (see Fig. B10 in Appendix B). For the pumping rate this was achieved after four to five full impeller rotations $n\,t$; up to 50 rotations were necessary for the circulation rate. Discretization schemes and solvers were identical to the ones described in [54].

Since phase-averaged flow fields were obtained experimentally, analogous fields were derived from the CFD data for the single propeller case. For this, flow data were transformed to a cylindrical reference frame first. Fifty radial-axial planes with a regular grid of 500 × 500 points with an angle increment of 360°/51 in the bounds as given in Fig. 4 were then determined by interpolation and averaged.

4 Results and Discussion

4.1 Single Propeller

4.1.1 Flow Behavior

In Fig. 4, radial-axial flow fields normalized to the tip speed $w_{\mathrm{Tip}} = \pi\, dn$ are presented as contour plots with overlaying streamlines. The first column depicts experimental PIV, the second Newtonian (ne), the third Carreau-Yasuda (pp), and the last the viscoelastic model (ve) results. The stirring rate increases from top to bottom.

At the lowest stirring rate of $n = 100$ rpm, an axial pumping effect is generated in all fluids, but no clear axial jet is developed. A qualitative difference between inelastic and elastic fluids is evident: While the maximum axial velocity for the inelastic fluids (ne and pp) is found at about $rd^{-1} \approx 0.5$, this maximum is shifted to the axis of rotation for the elastic fluids (PIV and ve). This is also obvious in the corresponding radial profiles of the axial velocity shown in Fig. 5. Further, while velocity magnitudes are severely underestimated by the inelastic models, acceptable agreement is found between ve and PIV. The overestimation of flows calculated with the Giesekus model can mainly be attributed to the fitting procedure, which resulted in an overestimation of the primary normal stress differences as explained above (cf. Sect. 3.1).

Since the viscosities for pp and ve are similar, the differences in flow behavior clearly have to be attributed to the elasticity of the fluid. In [26, 30] we reasoned that the flow fields obtained for ve and PIV for $n = 100$ rpm are generated in elastically dominated flows. Here, radial gradients of the tangential velocity induce elastic normal stresses, which lead to elastic forces pointing to the axis of rotation. These additional elastic forces induce a radial transport of fluid towards the propeller and, therefore, increase axial pumping rates due to continuity. This reasoning is supported by the flow fields, which show radial velocity components for $zd^{-1} < 0$ towards the agitator in the elastic fluids. No such radial transport takes place for the inelastic fluids (cf. Fig. 4, 100 rpm).

Increasing the stirring rate to $n = 500$ rpm, no significant change of the normalized flow fields is found for the elastic fluids (cf. Fig. 4, 500 rpm, both PIV and ve). In [30] we reported on the self-similarity of flows in the elastically

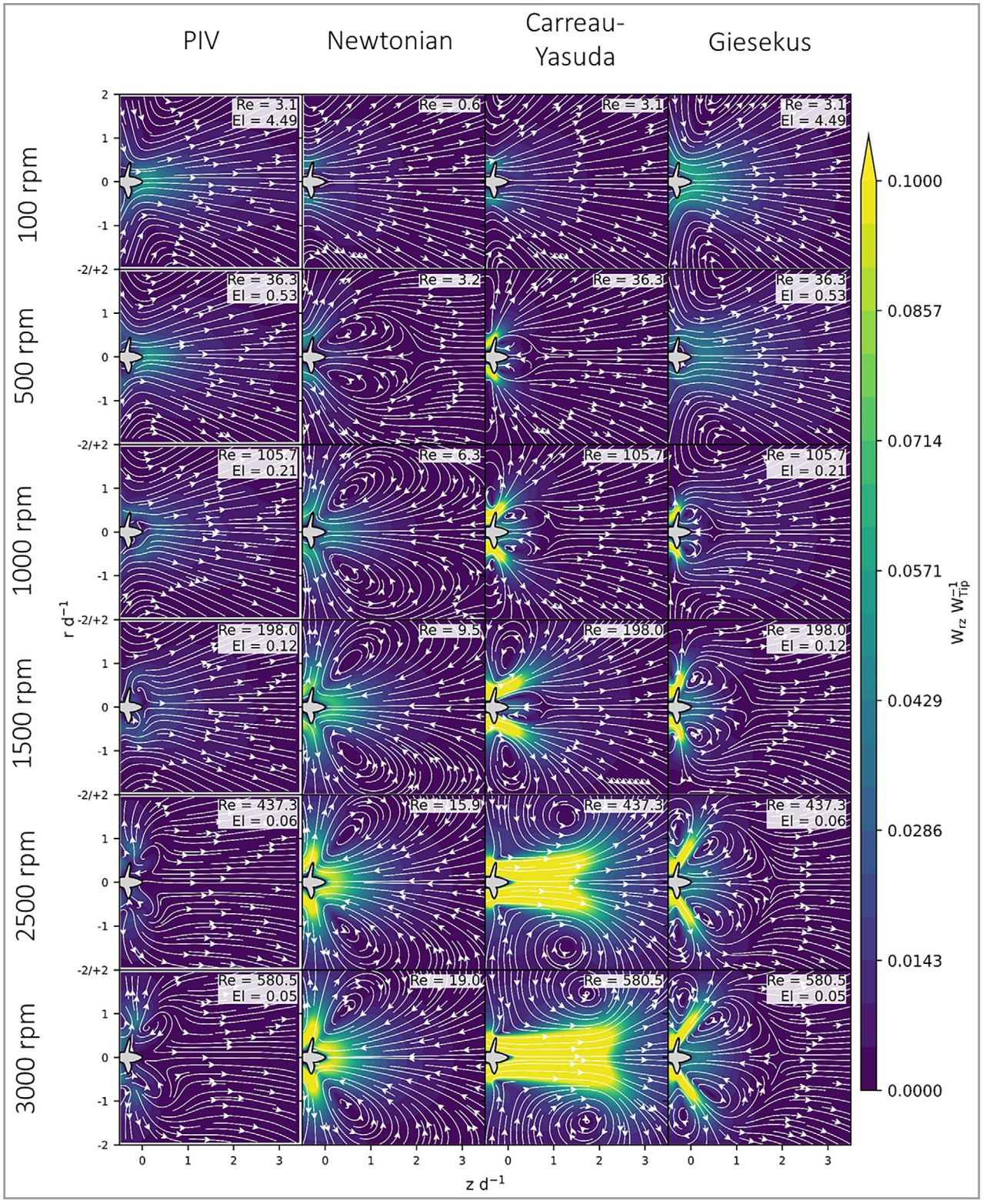

Figure 4. Experimentally and numerically obtained flow fields in the single-propeller configuration. Dimensionless numbers for the non-Newtonian fluids are calculated with k_{MO}.

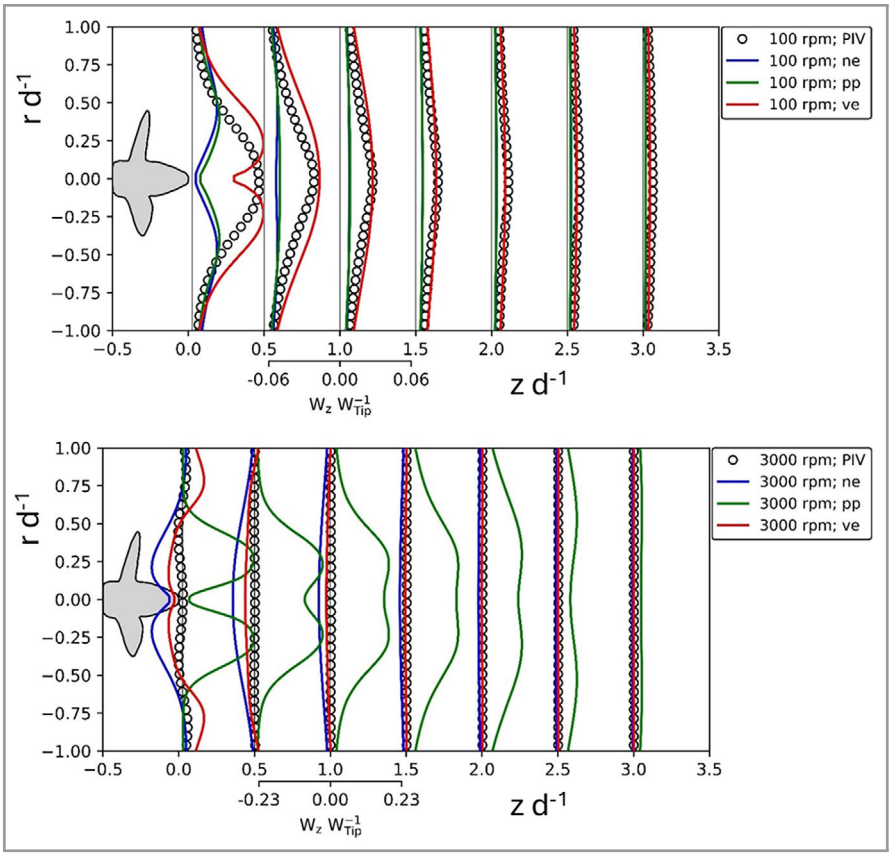

Figure 5. Experimentally and numerically obtained radial profiles of the axial velocity for different axial distances.

dominated regime in a centrally stirred tank. The results here support this finding and show that this phenomenon also takes place in other mixer geometries. Distinct changes in flow behavior occur for the inelastic fluids, which, therefore, differ markedly from the experimental results. An additional radial discharge component is found in both ne and pp, leading to semi-radial discharge and a recirculation zone in front of the propeller. In [26] we hypothesized that this backflow region is a consequence of flow compartmentalization resulting from regions which are either elastically or inertially dominated. Its existence in inelastic fluids suggests instead that the backflow region is simply a consequence of the semi-radial flow patterns, in which backflow of fluid occurs due to continuity.

At $n = 1000$ rpm, a fully radial flow field is generated in the Newtonian fluid which is maintained for all other analyzed stirring rates (cf. Fig. 4, ne, 1000–3000 rpm). For pp, an increase of the stirring rate leads to a gradual collapse of the semi-radial to a fully axial discharge angle, so that a fully developed axial propeller jet is eventually generated at n = 2500 rpm (cf. Fig. 4, pp, 500–3000 rpm). For the elastic fluids, the initial formation of a backflow region occurs at $n =$ 1000 rpm, albeit in a smaller size in the PIV data compared to ve. Increasing the stirring rate causes a growth of the backflow region in the elastic fluids. For ve, fully radial discharge for $n = 1500$ rpm and semi-radial flow for higher n is found. For PIV, radial flow is generated for $n \geq 2500$ rpm. Hence, significant differences are also detected between the Giesekus model and the PIV data for $n \geq 1500$ rpm. However, these deviations are much smaller compared to the pp model as also demonstrated in the flow profiles given in Fig. 5 (3000 rpm). The consideration of elastic properties, therefore, clearly leads to a significant improvement of the numerical results.

4.1.2 Flow Characteristics

In Fig. 6, pumping rates $\dot{V}_P$ are given determined by the methods explained in Sect. 2.2. $\dot{V}_P$ as function of the stirring rate is strongly influenced by the rheology of the fluid (see Fig. 6a). Negative pumping rates are determined for $n \geq 1000$ rpm in the Newtonian fluid resulting from the radial flow behavior. For pp, high positive pumping rates are generated for $n \geq 1500$ rpm, i.e., when the initial collapse of the radial flow to an axial jet takes place. The results for the viscoelastic fluids are located between ne and pp: Pumping rates are positive for $n \leq 1000$ (1500) rpm for ve (PIV) and negative for higher stirring rates. Again, these results indicate that considering elasticity in the models leads to significantly improved numerical results.

A plot over Re, calculated with k_{MO} (Eq. (12)) and the Carreau-Yasuda equation (Eq. (6)) for the non-Newtonian fluids and with a constant viscosity η_0 for the Newtonian fluid, allows to derive some categorizations of the flow behavior of the inelastic fluids, but not for the elastic fluids (see Fig. 6b). Radial flow patterns are obtained for $3 < Re < 20$, semi-radial for $36 < Re \leq 198$, and axial jets for $Re > 198$. These numbers agree well to the results described in [21], in which radial flow behavior was found for $Re = 15$ and 35 in the Newtonian fluid and semi-radial flow for $20 < Re_y < 200$, where Re_y is the yield stress Reynolds number, in the shear-thinning fluids exhibiting a yield stress.

For the elastic fluids, a categorization with El is more meaningful since flows are affected more by N_1 than τ_s ($Wi > 1$, see Fig. 2a). A corresponding plot of the pumping number Fl_P, separated into a negative and positive flow number determined by evaluating either the negative or positive flow, is given in Fig. 6c. Hence, fully positive axial flow is

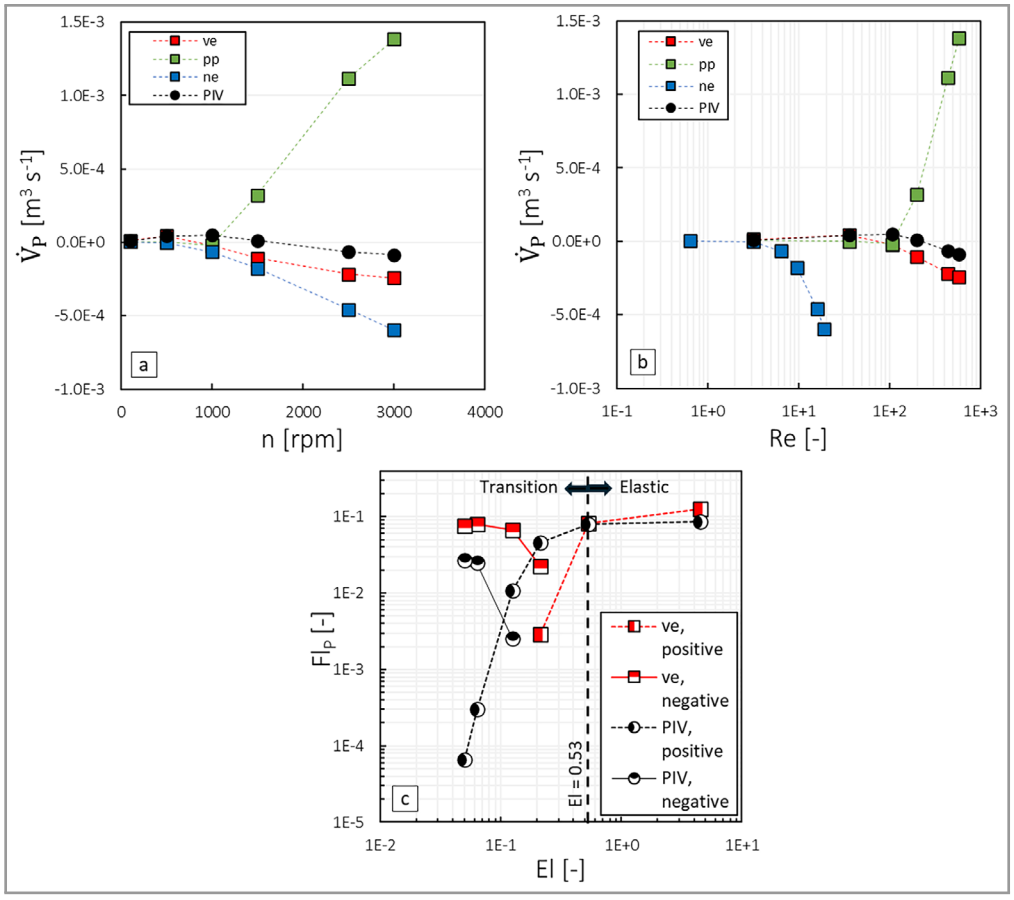

Figure 6. Pumping rates or respective flow numbers given as function of stirring rate (a), Reynolds number (b), and elasticity number (c).

obtained for $El \geq 0.53$ with a constant $Fl_P \approx 0.1$ resulting from the self-similarity of flows. This threshold value is similar to the threshold value of $El \geq 0.63$ we found for elastically dominated flow in a centrally stirred tank with axial impellers with much larger diameters ($d = 0.1$ m and $d = 0.135$ m) [30]. It further agrees with the threshold value of $El \geq 0.54$ (disregarding the blade pitch angle correction applied in [26]) found for a pilot-scale biogas fermenter agitated by side-entry propeller agitators (0.1 m $\leq d \leq$ 0.175 m) as described in [26]. This suggests that the threshold value for the elastic regime is virtually independent of vessel shape and agitator scale, which agrees well with the findings described in [52].

For $El < 0.53$, a backflow region and, hence, negative flow is generated. In [26] we described that for $El < 0.05$ this region disappears. This value is not supported by the data determined in this study (cf. Fig. 6c); it is likely the El range for which backflow occurs is also dependent on the agitator geometry.

4.2 Multipropeller Configuration

Since the results discussed in Sect. 4.1 are focused on the propeller vicinity, effects of rheology on the large-scale flow in a fermenter can not be derived. Hence, simulations were also conducted for a geometry which is similar to industrial biogas fermenters (cf. Sect. 3.3). Corresponding results for the flow parallel to cutting plane $w_{xy}w_{Tip}^{-1}$ at the height of the propellers are given in Fig. 7. Additionally, a section as indicated by the white square in Fig. 7, 500 rpm, pp, is given to visualize to flow close to the agitators.

In general, all phenomena close to the impeller as described for the single-propeller configuration are also evident in this mixer geometry. For pp, an axial pumping effect without a jet is found for 500 rpm. Increasing the stirring rate leads to semi-radial flow with a back flow region first, until for $n = 6000$ rpm a fully developed axial jet is generated. This jet leads to high pumping rates $\dot{V}_P$ (see Fig. 8a). Note that the stirring rate values for the flow transitions differ from the single-propeller configuration since a smaller propeller ($d = 0.02$ m) was used for the multipropeller configuration. For ve, an axial pumping effect is found for $n \leq$ 1500 rpm with much higher $\dot{V}_P$ compared to pp (see Fig. 8a). This can again be attributed to elastically dominated flow.

Resulting from elastic normal stresses, axial flow maxima are again located at the axis of rotation and fluid is mainly drawn in radially, which even leads to fluid being discharged behind the propeller under these conditions. The elasticity, therefore, not only causes quantitative differences, but alters

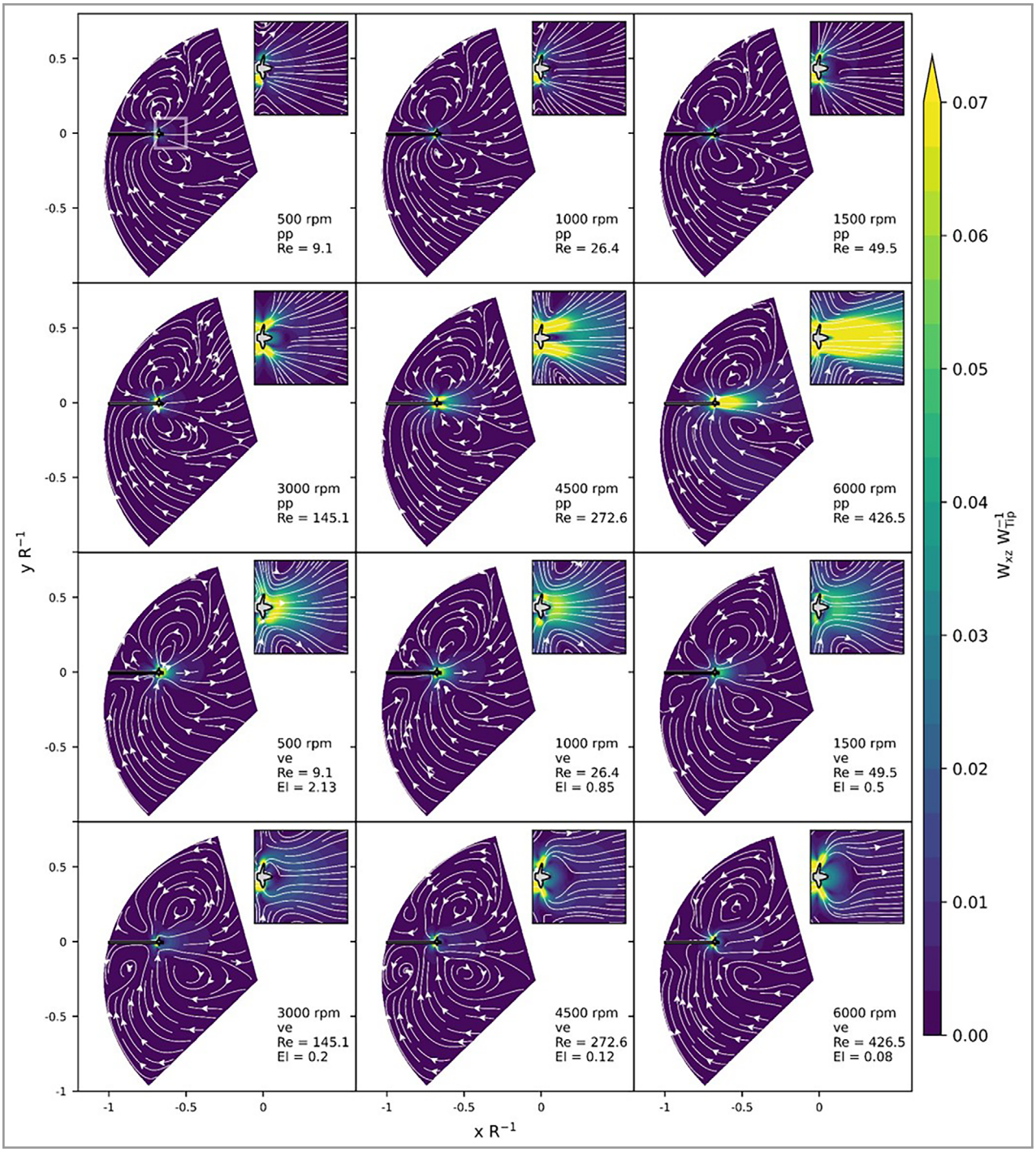

Figure 7. Numerically obtained flow fields in the *x*-*y*-plane at height of the propellers. Detailed view of the vicinity of the propeller in bounds as given by the white square for 500 rpm, pp.

the mechanism of how fluid is transported by a propeller. A self-similarity of these flows is also generally evident, but since no phase averages were determined here, some differences exist due to different orientations of the propeller blades to the cutting plane. For $n \geq 3000$ rpm, radial discharge and a backflow region is generated in the viscoelastic fluid.

For all analyzed conditions, fluid is exchanged between the three different sections in a primary circulation vortex. The rates of this primary circulation flow $\dot{V}_C$ are given

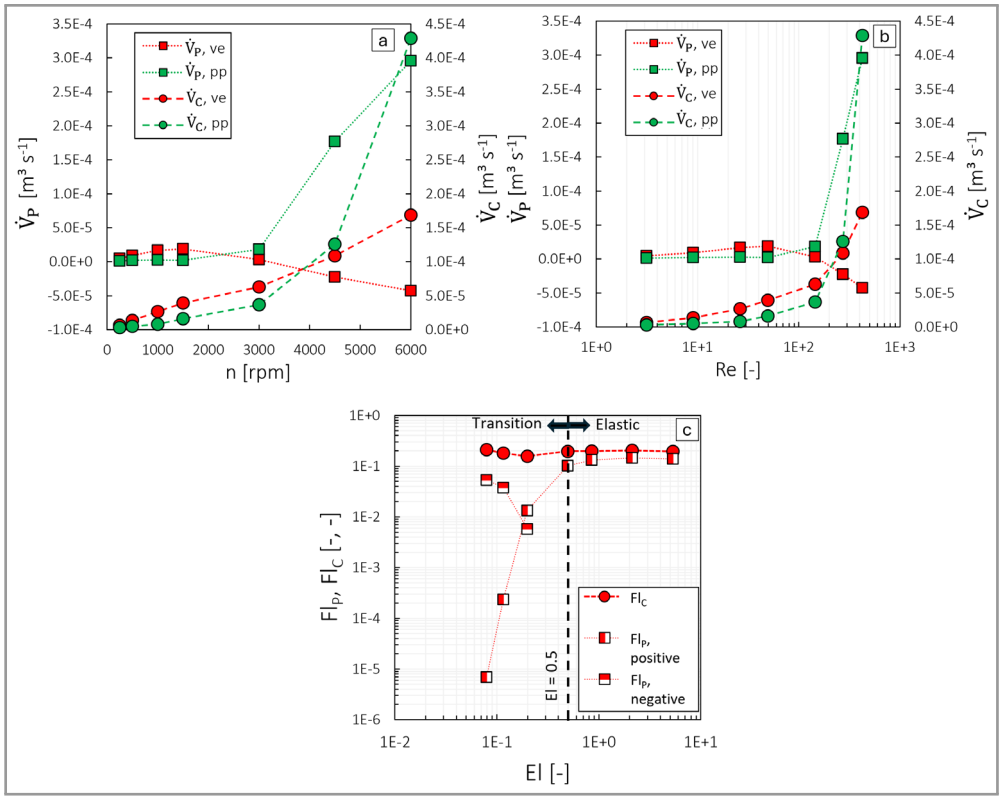

Figure 8. Pumping and circulation rates (or respective flow numbers) given as function of stirring rate (a), Reynolds number (b), and elasticity number (c).

in Fig. 8. For stirring rates $n \leq 3000$ rpm, a significant enhancement of the circulation flow rate is found for the elastic fluid compared to pp. Markedly higher rates are generated in pp for $n = 6000$ rpm compared to ve due to the formation of an axial propeller jet: $\dot{V}_C$ in pp is 2.26 times higher than in ve. This deviation is of similar magnitude to the overestimation of flows by the inelastic models in the industrial-scale fermenter (cf. Sect. 1.3). While this does not necessarily mean that the deviations in the industrial-scale fermenter are due to the disregard of elasticity, it certainly shows the potential of improvements possible by the usage of viscoelastic models. Further, considering that mixing times are mainly dependent on $\dot{V}_C$ in stirred tanks with side-entering impellers [26], the formation of propeller jets, which is suppressed by the elasticity of the fluid, is highly desirable for an effective mixing process. The elasticity, therefore, severely complicates mixing in a fermenter.

From Fig. 8b, it is again evident that *Re* is incapable of categorizing flows affected by elasticity. For the inelastic fluid, similar threshold values for the flow regime transitions are found in the multipropeller configuration, e.g., axial jets are generated at $Re \geq 272$. For the elastic fluid, a categorization with *El* is again more meaningful and virtually identical threshold values to the single propeller configuration can be given (cf. Fig. 8c): For $El \geq 0.5$, flow is elastically dominated and can be scaled to *n*, which results in constant flow numbers for both pumping Fl_P and circulation Fl_C. For lower *El*, radial flow components and, hence, a backflow region develops, which leads to a slight reduction of Fl_C at $El = 0.2$.

5 Conclusion

To obtain a better understanding of how pseudoplasticity and elasticity influence propeller and the corresponding circulation flow in biogas fermenters, simulations with Newtonian as well as inelastic and elastic shear-thinning fluids were conducted. For this, parameters for different rheological models were derived from rheological measurements of a viscoelastic CMC solution. CFD results from these models were compared to experimental PIV data.

For the inelastic fluids, flow behavior is determined by the balance of viscous and inertial forces as expressed by the Reynolds number: In the low transitional regime, radial flow patterns are developed, limiting the pumping rate of propellers. Increasing the stirring rate and, thereby, the ratio of inertial to viscous forces, successively more axial flow components are induced by the propellers, so that for sufficiently high stirring rates fully developed axial jets are formed. These jets significantly increase the circulation rate in a fermenter and are, thus, highly beneficial for an effective mixing operation.

The elasticity severely affects how a fluid is transported by a propeller. In elastically dominated flows, the main

mechanism of fluid transport is induced by elastic normal stresses caused by radial gradients of the tangential velocity, which lead to a radial transport of fluid towards the propeller and, thus, increase axial pumping rates compared to inelastic fluids. Further, elasticity suppresses the formation of axial jets, i.e., higher stirring rates are necessary to induce axial jets than in inelastic fluids. Considering that these jets are critical for an effective mixing process, the elasticity severely complicates mixing in a fermenter. The type of flow generated by a propeller in a viscoelastic fluid depends on the force balance of elastic forces, induced by elastic normal stresses, to inertial forces. This balance is described by the elasticity number.

Further, significantly improved qualitative and quantitative agreement between simulation and PIV data is found for the viscoelastic model compared to the inelastic approaches. In the elastically dominated regime, flows are reproduced with an acceptable quantitative agreement by the Giesekus model. Improvements could be achieved with a more accurate set of model parameters. Here, the consideration of secondary normal stress differences and inconstant elongational viscosities could also help in improving the simulation results further.

A logical next research step would be the consideration of elasticity also for the simulation of industrial-scale biogas fermenters. For this, reliable measurement methods need to be developed first which are capable of quantitatively determining elastic properties of biogenic substrates. It should also be tested if other viscoelastic models like Phan-Thien-Tanner or FENE-P can reproduce viscoelastic flows more accurately than the Giesekus model.

Acknowledgment

This work was funded by the Bundesministerium für Ernährung und Landwirtschaft (BMEL, Germany) via Fachagentur Nachwachsende Rohstoffe (FNR, Germany, grant numbers: 22402017, 2219NR437). We would like to thank the students Alejandro Hackelbusch, Aline Luxa, Bernhard Tontarra, and Michael Drantmann for conducting many simulations for their Bachelor or Master theses. The experimental work with the PIV method conducted by Manuel Brehmer for his PhD thesis is highly appreciated.

Open access funding enabled and organized by Projekt DEAL.

Appendix A

In Fig. A1, unordered, average pumping rates $\dot{V}_{P,avg}$ in dependence of the number of quasi-instantaneous flow fields N used for phase-averaging are given to evaluate the statistical validity of the phase-averaged PIV flow fields.

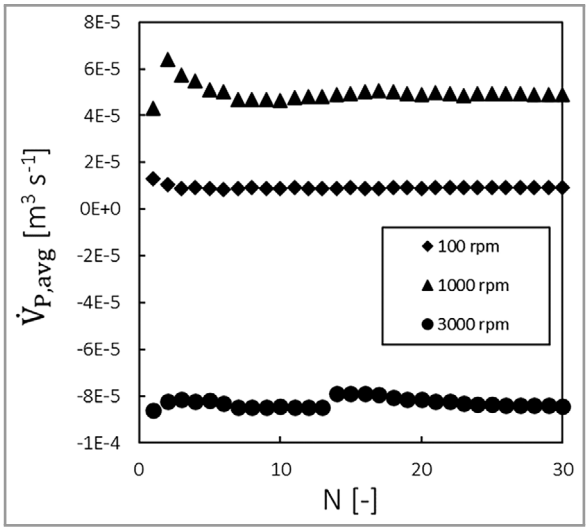

Figure A1. Average pumping rates in dependence of the number of quasi-instantaneous flow fields used for phase-averaging.

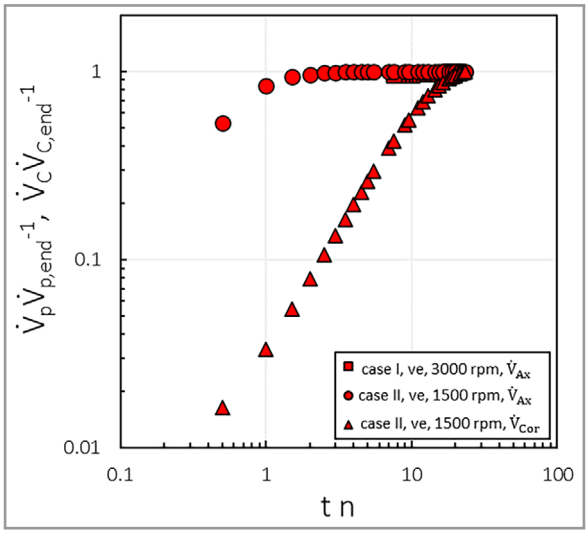

Figure B1. Time dependence of simulated pumping and circulation rates. Case I denotes the single-propeller, case II the multipropeller configuration.

Appendix B

In Fig. B1, typical time-dependent pump- and circulation rates relative to the values determined for the last time step $\dot{V}_P\dot{V}_{P,end}^{-1}$ and $\dot{V}_C\dot{V}_{C,end}^{-1}$ are given as function of the number of propeller rotations $t\ n$.

Symbols used

A	[m^2]	area
A_D	[m^2]	disk area

a	[–], [Pa s^{3+b}]	Carreau-Yasuda model parameter, power-law parameter
b	[–]	power-law parameter
Co	[–]	Courant number
D	[m]	vessel diameter
$\boldsymbol{D}$	[s^{-1}]	rate of deformation tensor
d	[m]	impeller diameter
El	[–]	elasticity number
Fl_C	[–]	circulation flow number
Fl_P	[–]	pumping flow number
G'	[Pa]	storage modulus
G''	[Pa]	loss modulus
H	[m]	vessel height
k_{MO}	[–]	Metzner-Otto constant
L	[m]	vessel length
N	[–]	number of elements or modes
N_1	[Pa]	primary normal stress difference
n	[–], [rpm]	Carreau-Yasuda model parameter, rotational frequency
p	[Pa]	pressure
R	[m]	vessel radius
r	[m]	radial distance coordinate of a cylindrical coordinate system
Re	[–]	Reynolds number
Re_Y	[–]	yield-stress Reynolds number
t	[s]	time
$\dot{V}_C$	[$m^3 s^{-1}$]	circulation flow rate
$\dot{V}_P$	[$m^3 s^{-1}$]	pumping rate
W	[m]	vessel width
Wi	[–]	Weissenberg number
$\boldsymbol{w}$	[m s^{-1}]	velocity vector
w_{Tip}	[m s^{-1}]	impeller tip speed
x	[m]	x variable of a cartesian coordinate system
y	[m]	y variable of a cartesian coordinate system
z	[m]	z variable of a cartesian and cylindrical coordinate system

Greek letters

α	[–]	Giesekus mobility factor
$\dot{\gamma}$	[s^{-1}]	shear rate
η	[Pa s]	dynamic viscosity
η_0	[Pa s]	dynamic viscosity at zero shear rate
η_∞	[Pa s]	dynamic viscosity at infinite shear rate
θ	[°]	azimuthal angle
λ	[s]	relaxation time
λ_{CY}	[s]	Carreau-Yasuda relaxation time
λ_ω	[s]	characteristic relaxation time
ν	[$m^2 s^{-1}$]	kinematic viscosity
ρ	[kg m^{-3}]	density
ω	[rad s^{-1}]	rotational frequency
$\boldsymbol{\tau}$	[Pa]	stress tensor
$\boldsymbol{\tau}_P$	[Pa]	elastic part of the extra-stress tensor
$\boldsymbol{\tau}_S$	[Pa]	inelastic part of the extra-stress tensor
τ_S	[Pa]	shear stress
ψ_1	[Pa s^2]	primary normal stress coefficient

Sub- and superscripts

avg	average
end	final time step
i	sum index

Abbreviations

CFD	computational fluid dynamics
CMC	carboxymethyl cellulose
ne	Newtonian
PIV	particle image velocimetry
pl	power-law
pp	pseudoplastic
ve	viscoelastic

References

[1] N. Schneider, M. Gerber, *Renewable Sustainable Energy Rev.* **2020**, *121*, 109709.
[2] J.-C. Baudez, R. K. Gupta, N. Eshtiaghi, P. Slatter, *Water Res.* **2013**, *47*, 173–180.
[3] E. Farno, J. C. P. R. Baudez, N. Eshtiaghi, *Chem. Eng. J.* **2016**, *304*, 362–368.
[4] J. Jiang, J. Wu, S. Poncin, H. Li, *Biochem. Eng. J.* **2014**, *86*, 57–61.
[5] M. Brehmer, M. Kraume, *Czasopismo Techniczne* **2016**, *113*, 33–42.
[6] M. Brehmer, *Dissertation*, Technische Universität Berlin **2021**.
[7] N. Q. Dzuy, D. V. Boger, *J. Rheol.* **1983**, *27* (*4*), 321–349.
[8] L. Kamkeng, P. Marchal, A. Bertrandias, B. Le Creurer, E. Olmos, *Chem. Eng. Res. Des.* **2023**, *196*, 309–318.
[9] C. Ford, F. Ein-Mozaffari, C. Bennington, F. Taghipour, *AIChE J.* **2006**, *52* (*10*), 3562–3569.
[10] S. Saeed, F. Ein-Mozaffari, S. Upreti, *Ind. Eng. Chem. Res.* **2007**, *46* (*7*), 2172–2179.
[11] M. Bhole, C. Ford, C. Bennington, *Chem. Eng. Res. Des.* **2009**, *87* (*4*), 648–653.
[12] M. Bhole, C. Bennington, *Ind. Eng. Chem. Res.* **2010**, *49* (*9*), 4444–4451.
[13] S. Bhattacharya, C. Gomez, A. Soltanzadeh, F. Taghipour, C. Bennington, G. Dumont, *Can. J. Chem. Eng.* **2010**, *88* (*2*), 295–305.
[14] J. Sossa-Echeverria, F. Taghipour, *Ind. Eng. Chem. Res.* **2012**, *51*, 15258–15267.
[15] F. Ein-Mozaffari, S. R. Upreti, *Chem. Eng. Res. Des.* **2009**, *87*, 515–523.
[16] D. Fernandes del Pozo, A. Liné, K. M. Van Geem, C. Le Men, I. Nopens, *AIChE J.* **2020**, *66* (*6*), e16939.

[17] D. Patel, F. Ein-Mozaffari, M. Mehrvar, *IOP Conf. Ser.: Mater. Sci. Eng.* **2012**, *42* (*1*), 012048.
[18] W. Kelly, B. Gigas, *Chem. Eng. Sci.* **2003**, *58* (*10*), 2141–2152.
[19] L. Pakzad, F. Ein-Mozaffari, S. R. Upreti, A. Lohi, *Can. J. Chem. Eng.* **2013**, *91* (*1*), 90–100.
[20] L. Adams, M. Barigou, *Chem. Eng. Res. Des.* **2007**, *85* (*5*), 598–604.
[21] J. Sossa-Echeverria, F. Taghipour, *Ind. Eng. Chem. Res.* **2012**, *51*, 15258–15267.
[22] M. Brehmer, T. Eppinger, M. Kraume, *Chem. Ing. Tech.* **2012**, *84* (*11*), 2048–2056.
[23] T. Reviol, S. Kluck, M. Böhle, *Chem. Eng. Sci.* **2018**, *190*, 320–332.
[24] P. Wang, T. Reviol, H. Ren, M. Böhle, *Exp. Therm. Fluid Sci.* **2019**, *109*, 109866.
[25] P. Wang, T. Reviol, H. Ren, M. Böhle, *Chem. Eng. Res. Des.* **2019**, *147*, 259–277.
[26] M. Kolano, J. Danke, M. Kraume, *Biomass Bioenergy* **2021**, *152*, 106180.
[27] C. Cao, M. Kraume, *Chem. Eng. Sci.* **2020**, *223*, 115750.
[28] C. Cao, M. Kraume, *Chem. Eng. Sci.* **2021**, *235*, 116506.
[29] A. Story, Z. Jaworski, M. J. Simmons, E. Nowak, *Chem. Pap.* **2018**, *72* (*3*), 593–602.
[30] M. Kolano, M. Kraume, *Chem. Eng. Sci.* **2023**, *282*, 119301.
[31] J. Wang, Q. Xue, T. Guo, Z. Mei, E. Long, Q. Wen, H. Wei, T. Luo, R. Huang, *Renewable Sustainable Energy Rev*. **2018**, *97*, 64–73.
[32] A. R. T. Saini, K. Paritosh, K. V. N. Pareek, D. Tripathi, V. Vivekanand, *Bioengineered* **2021**, *12* (*1*), 6418–6433.
[33] C. Sadino-Riquelme, R. E. Hayes, D. Jeison, A. Donoso-Bravo, *Crit. Rev. Environ. Sci. Technol.* **2018**, 1–38.
[34] I. Nopens, D. Sudrawska, W. Audenaert, D. Fernandes del Pozo, U. Rehman, *Water Sci. Technol.* **2020**, *81* (*8*), 1636–1645.
[35] H. Caillet, A. Bastide, L. Adelard, *Cleaner Waste Syst*. **2023**, *6*, 100124.
[36] C. D. Bastiani, D. Kennedy, A. Reynolds, *Water Res*. **2023**, *242*, 120220.
[37] B. Ohnmacht, P. Kress, H. Oechsner, A. Lemmer, *Biomass Bioenergy* **2020**, *139*, 105613.
[38] B. Ohnmacht, A. Lemmer, H. Oechsner, P. Kress, *Bioresour. Technol.* **2021**, *332*, 125099.
[39] P. Kress, H.-J. Nägele, A. Lemmer, B. Kolb, *Landtechnik* **2020**, *75* (*2*), 35–50.
[40] https://www.fnr.de/projektfoerderung/projektdatenbank–der–fnr/projektverzeichnis–details?fkz=2219NR437&cHash=79fe44c0e7a22d4473b4044fff9a3a8c (Accessed on May 07, 2024)
[41] R. Poole, *J. Non-Newtonian Fluid Mech.* **2023**, *320*, 105106.
[42] K. Yasuda, R. Armstrong, R. Cohen, *Rheol. Acta* **1981**, *20*, 163–178.
[43] R. G. Larson, *Constitutive Equations for Polymer Melts and Solutions*, 1st ed., Butterworths Series in Chemical Engineering, Stoneham **1988**.
[44] H. Giesekus, *J. Non-Newtonian Fluid Mech.* **1982**, *11* (*1*), 69–109.
[45] H. Giesekus, *J. Non-Newtonian Fluid Mech.* **1983**, *12* (*3*), 367–374.
[46] M. Kraume, *Mischen und Rühren: Grundlagen und moderne Verfahren*, Wiley-VCH, Weinheim **2002**.
[47] A. Metzner, R. Otto, *AIChE J*. **1957**, *3* (*1*), 3–10.
[48] J. Jiang, J. Wu, S. Poncin, H. Z. Li, *Process Biochem*. **2016**, *51* (*3*), 345–351.
[49] F. Maluta, F. Alberini, A. Paglianti, G. Montante, *Chem. Eng. Res. Des.* **2024**, *205*, 498–509.
[50] A. Nienow, T. Elson, *Chem. Eng. Res. Des.* **1988**, *66* (*11*), 5–15.
[51] N. Özcan-Taskin, A. Nienow, *Food Bioprod. Process.* **1995**, *73* (*2*), 49–56.
[52] M. Kolano, M. Kraume, *Chem. Eng. Tech.* **2019**, *42* (*8*), 1670–1679.
[53] A. Nienow, *Chem. Eng. Sci.* **1997**, *52* (*12*), 2557–2565.
[54] M. Kolano, L. Böhm, M. Kraume, *J. Non-Newtonian Fluid Mech.* **2024**, submitted.
[55] S. Annas, H.-A. Jantzen, J. Scholz, U. Janoske, *Chem. Eng. Tech.* **2018**, *41* (*4*), 739–746.
[56] S. Annas, M. Elfering, H.-A. S. J. Jantzen, U. Janoske, *Chem. Eng. Sci.* **2022**, *258*, 117767.
[57] L. Megue Kamkeng, C. Loubière, O. Dufaud, P. Marchal, B. Le Creurer, E. Olmos, *Chem. Eng. Sci.* **2024**, *298*, 120299.
[58] J. Favero, A. Secchi, N. S. M. Cardozo, H. Jasak, *J. Non-Newtonian Fluid Mech.* **2010**, *165* (*23–24*), 1625–1636.
[59] M. Bhole, L. Hui, C. Gomez, C. Bennington, G. Dumont, *Can. J. Chem. Eng.* **2011**, *89* (*5*), 985–995.

